1-1-2012

Dc slice imaging, crossed beam reaction of chlorine radical with butane

Tarek Oussama Abdul ghani
Wayne State University,

DC SLICE IMAGING, CROSSED BEAM REACTION OF CHLORINE RADICAL WITH BUTANE

by

TAREK ABDUL GHANI

THESIS

Submitted to Graduate School

of Wayne State University,

Detroit, Michigan

in partial fulfillment of requirements

for the degree of

MASTER OF SCIENCE

2012

MAJOR: CHEMISTRY

Approved by:

_____

Advisor Date

ACKNOWLEDGMENT

The list of people I want to thank for this is long and I truly appreciate all the help and support I received at Wayne State University. The person that I need to thank first and foremost is Dr. Arthur Suits. A man that was always willing to help me and has greatly affected my life for the better. Also the wonderful students in the suits group past and present they have always been supportive and helpful and friendly, and for that I am very grateful. I also want to thank Melissa Barton who helped me along the way. Finally I want to thank my wife Iman and my daughter Farah for making every day of my life interesting and an adventure.

TABLE OF CONTENTS

LIST OF TABLES

LIST OF FIGURES

CHAPTER 1 - INTRODUCTION

1.1 Introduction to Kinetics.

At the heart of every bimolecular gas phase reaction, is at least one collision between two molecules or atoms. Each collision in the process of transforming the reactants to products is an elementary step. The overall combination of elementary steps makes up the reaction mechanism, which must satisfy the overall balanced reaction equation. Because each elementary step is a collision of individual particles, a dynamic analysis of the reactive process is possible. Understanding the dynamics of chemical reactions is very important academically and to the advancement of many industries. The data collected during dynamics experiments help paint a picture of the forces that are acting on the system during the chemical reaction.

The field of chemical kinetics began in 1886, when Cato Maximilian Guldberg Peter Waage published the law of mass action, rate = $k\,[A]^{\alpha}\,[B]^{\beta}$.[1] k is the rate constant, [A] and [B] are the concentrations, lastly α and β are the reaction orders. The physical interpretation of k, the reaction rate constant, was still a mystery at the time and was solved experimentally for each reaction. With the development of the Arrhenius equation,[2] there was a relation between the rate constant and the temperature of the system. The Arrhenius equation also introduced the concepts of activation energy (E_a) and frequency or the pre-exponential factor (A). The activation energy is the spark that the reaction needs

to overcome a reaction barrier. These new concepts had a profound impact on the field of kinetics and for nearly a century chemists have used the Arrhenius equation, to plot the variance in the rate of reaction with temperature, to calculate the activation energy and pre-exponential factor of a reaction. The data has generated volumes of books about the elementary processes that could be isolated for any given macroscopic reaction. All the rate constants were determined for macroscopic systems at a controlled temperature. The data collected has been very useful to develop efficient synthesis techniques. The physical interpretation of the activation energy and pre-exponential factor where still not completely understood. Some systems do not follow Arrhenius behavior and have a non-linear or negative relation between rate constant and temperature, for these systems it is not possible to determine the activation energy and frequency factor of the reaction. The data collected from kinetics experiments, are average properties of the individual particles that make up the macroscopic system. The data is useful in making predictions about macroscopic systems but fails to give details of the individual encounters between reactants.[3] Information about the individual encounter between the molecules is lost in the averaging over the many energy states of the reactants. To experimentally examine the reaction dynamics we must reactively collide individual particles, with fixed velocity vectors and monitor the products velocity and direction.

1.2 Reactive Scattering

A crossed beam machine coupled with dc slice velocity map imaging was used to experimentally collide two particles and monitor the speed and direction of the reactants and products. The images produced are a snapshot of the reaction, from an axis perpendicular to the reaction plane, a short time after the reactive collision.

We are interested in the direction and translational energy of the particles before and after the reactive collision, therefore no secondary collisions must occur. The only way to ensure single collision conditions is to create a mean free path much larger than the distance a particle must travel from the collision region to the detector. This is achieved through differential pumping, reaching a rest pressure of 10^{-7} torr and an operational pressure of 10^{-5} torr. The molecular beams are created to cross at a 90° angle, and are pulsed at 10Hz. The gas is pulsed from a piezo valve, and expands supersonically into the vacuum. The expansion causes a cooling of the internal degrees of freedom in the gas. The rotational temperature of the molecules in the beam is below 5K and the vibrational temperature is 50k.[4] The velocity distribution of the gas is narrower compared to the distribution of gas molecules at room temperature. To better control the velocity of the reactants, a noble gas is used as a carrier gas. For example using helium gives a velocity of 2000m/s and using xenon gives a velocity of 340m/s. The use of a noble gas as a carrier, also serves to prevent clusters from forming in the molecular beam.

By measuring the velocities of the reactants and product, we can calculate the energy associated with the system. The results give details of the process that took place between the molecules, as new bonds are forming and old bonds are breaking.

A simple model that describes the collision of two particles is the elastic hard sphere model. In this model the particles do not interact until the distance between them is equal to the combined radius of the two spheres. When the hard spheres collide, they are impenetrable and repel each other infinitely at that point. After the collision the direction of the velocity vector changes but the magnitude stays the same. As the particles fly towards each other the effective area of particle 1 as seen by particle 2, determines the probability of collision. The combined radius of the particles forms this effective area around each sphere. This area is the cross section and it is the effective measure of the probability and therefore the rate of collision between two spheres. The cross section of a hard sphere is given by $\sigma_{12} = \pi d^2$. Figure 1 shows the relationship between the cross section and the radius of the colliding spheres.

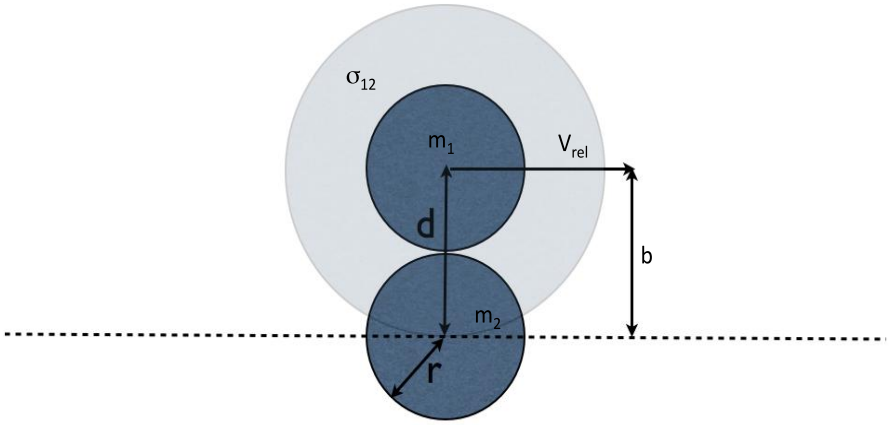

Figure 1 The relationship between the cross section and the radius of the hard spheres

When the distance of closest approach, the impact parameter (b), as measured perpendicularly to the velocity vector of the particles, is smaller than d a collision occurs. For real molecules d is not a fixed distance; rather it is an effective range of interaction. As the hard spheres approach each other we can use b to specify the approach of the particles.

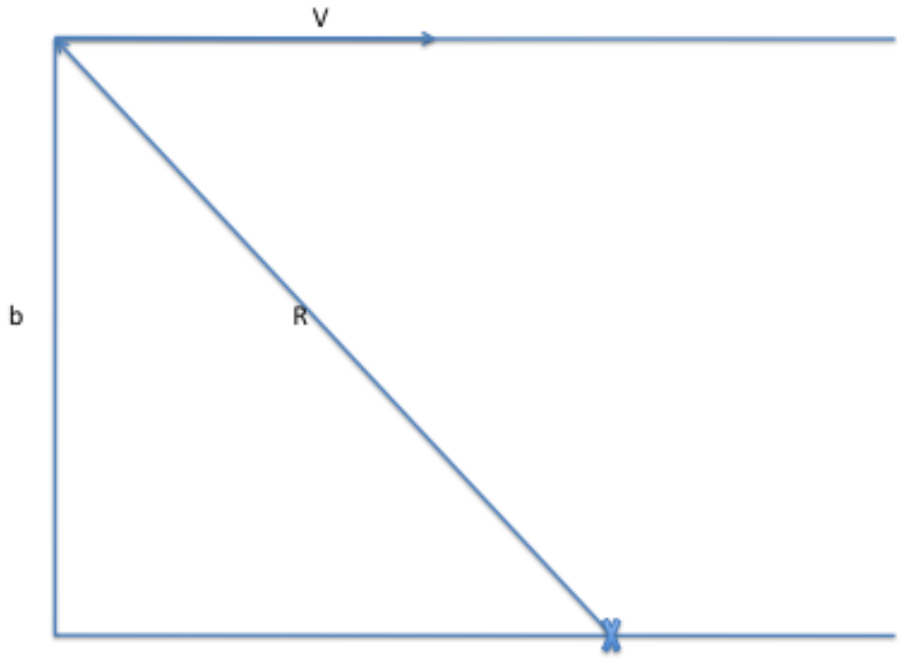

Figure 2 The relative position vector R and velocity v, at large separation.

To describe the relative motion of two particles we will use the relative position vector (R) separating the two particles, the relative velocity vector (V) and the impact parameter (b) shown in Figure 2. When b = 0 the particles collide head on, as the impact parameter gets larger, the less of it is in the component of the velocity vector that is directed along the R vector, and the more likely the particles will miss each other. The total energy of the system at a large

separation can be calculated from the equation $E_t = ½\mu V^2$, where $\mu = m_1m_2 / m_1+m_2$ is the Reduced mass.

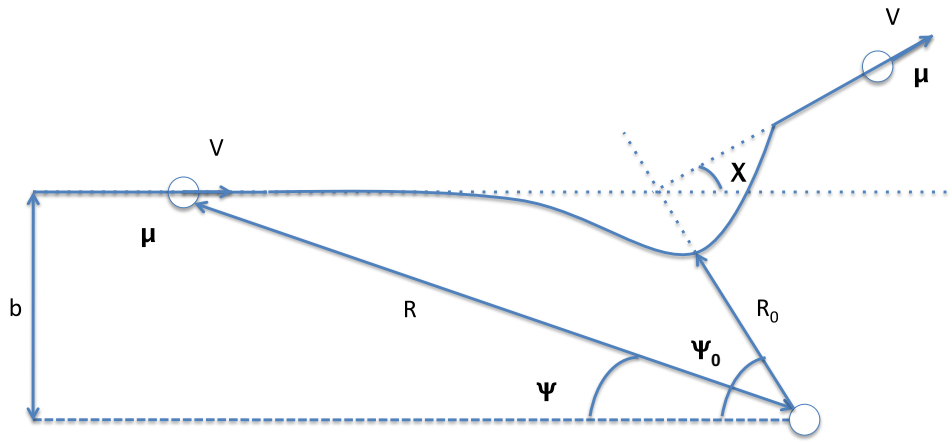

Figure 3 The collision trajectory in the center of mass frame.

The angle made by V and R is very important, this relation is shown in Figure 3. Also shown are the distance of closest approach (R_0) and the deflection angle (χ) between the initial and final relative velocity vectors. As the particles approach each other, both R and ψ change with time. The change in the position vector and the change in the orientation of this vector, have energy associated with each of them. The kinetic energy of the particles can now be written as, $E_{Ktotal} = ½\mu(dR/dt)^2 = ½\mu[(dR/dt)^2 + R^2 (d\psi/dt)^2]$. The first term is the translational

kinetic energy along the line of centers and the second is the centrifugal energy. The centrifugal energy will act as a force keeping the molecules apart. Measuring the change in both R and ψ will be an effective measure of the forces acting when the particles collide. To solve for $d\psi/dt$, we use the conservation of angular momentum. $L_{\text{pre-collision}} = \mu v b = L_{\text{post-collision}} = (d\psi/dt)\mu R^2$ and solving gives, $(d\psi/dt) = bv/R^2$.

During the collisions of real molecules the energy term also involves the potential energy term between the particles. This energy term is weakly attractive at along range and strongly repulsive at a short distance. The potential energy term is commonly combined with the centrifugal energy term to give an effective potential energy term, $E_{total} = \frac{1}{2}\mu(dR / dt)^2 + V_{eff}(R)$. For reactive scattering the change in energy between the reactant and products $E_{Rxn,}$ must also be taken into consideration. The total energy term becomes, $E_{total} = \frac{1}{2}\mu(dR/dt)^2 + V_{eff}(R) + E_{Rxn}$.

Using velocity map imaging, we can image the velocity vectors of the reactants and products in the center of mass. By comparing the velocity vectors and using the conservation of energy and momentum we ascertain the dynamics.

1.3 Frame of reference

It is clearly visible when looking at images produced from our scattering experiment, that the post collision velocity vectors are centered on a point. This point is the center of mass (cm) of the system. One of the most remarkable aspects of dc slice imaging as used in crossed beam experiments, is that you directly see the cm of the system. The cm of the system moves with the direction of movement of the system at a fixed velocity V_{cm}. Measuring the product velocity vector relative to the center of mass, will simplify the kinematics of the collision.

The center of mass reference frame is a reference frame in which the reference point is travelling on the cm of the system. In the cm frame the reactants appear to undergo a direct collision at the center of mass. The total momentum in this reference frame is always zero. This allows the determination of the velocity of the other particle that is not imaged. Another benefit of using this reference frame is that it is not dependent on the laboratory velocity of the reactants. Being independent of experimental geometry, allows results from different types of experiments to be compared, and also provides a much more intuitive picture of the collision dynamics. For these reasons, the scattering direction and translational energy is measured in the center of mass frame.

The reactant velocity vector is measured in the laboratory frame and the product velocity is measured in the center of mass frame. Before the collected data can be analyzed we must convert the laboratory velocity into the cm

velocity. A simple diagram that is conventionally used in the transformation is the Newton diagram Shown below.

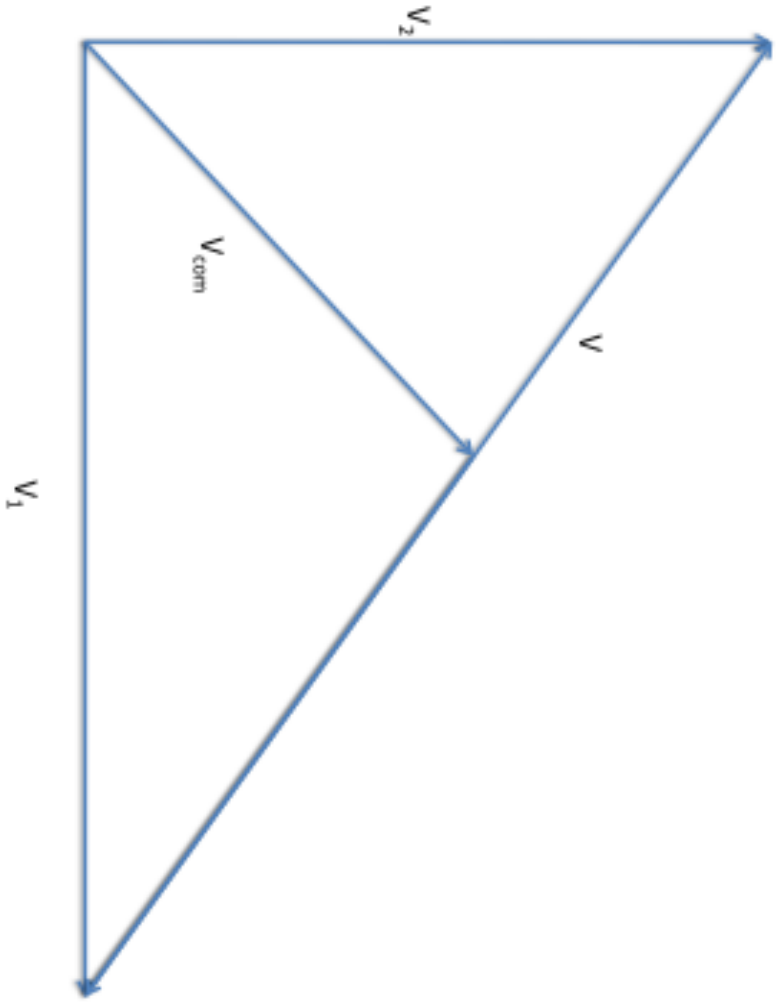

Figure 4 Newton diagram

Figure 4 shows the initial lab measured velocity vectors of the reactants and shows how the relative velocity is related to the initial velocity vectors in the lab frame, $V = V_1 - V_2$. The velocity vector of the center of mass is also shown and is calculated as $V_{cm} = (m_1V_1 + m_2V_2)/ (m_1 + m_2.)$ The cm will travel closer to the heavier particle, and it divides the relative velocity into the relative velocity in the cm frame of the reactants designated by U1 and U2, also for the products U'_1 and U'_2 shown in Figure 5.

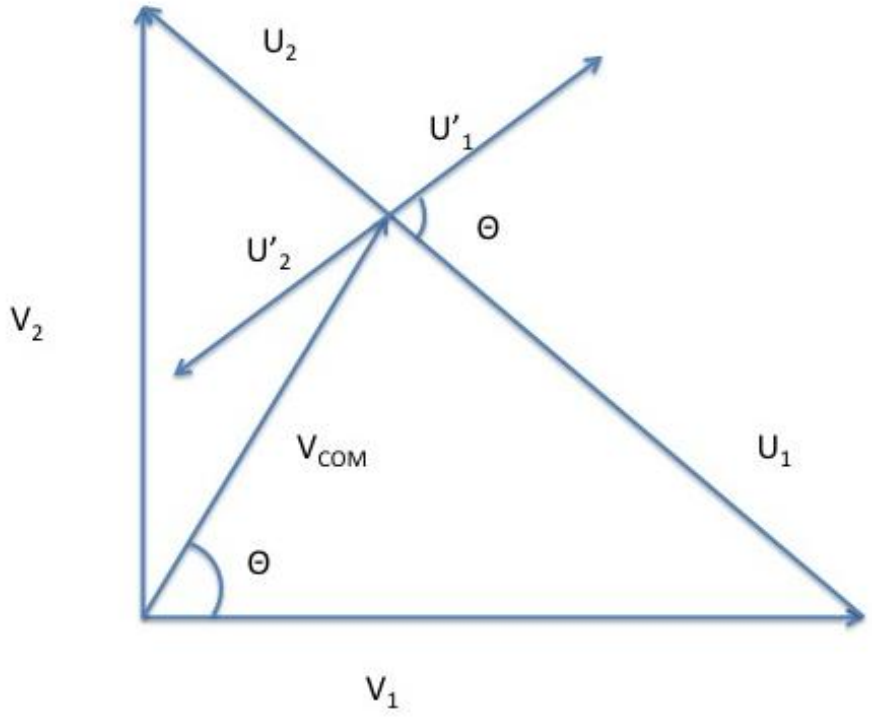

Figure 5 Newton diagram showing product scattering in the lab and COM frame.

The relative velocity in the cm frame is $V = U_1 - U_2 = V_1 - V_2$, as in the lab frame.[5] Using the relative velocity we calculate U1 and U2. $U_1 = Vm_2/(m_1+m_2)$ and $U_2 = Vm_1/(m_1+m_2)$. The laboratory velocity can be converted to the center of mass velocity simply by $V_{1lab} = V_{cm} + U_1$. Similarly for the products, $V'_{1lab} = V_{cm}+U'_{1.}$

Because the center of mass is moving, it has energy associated with it. It is therefore not involved in overcoming a reaction barrier, because it is the part of the velocity vector not in the reaction coordinates. That is, there are no forces acting on the center of mass of the system, so its motion is not involved in the reaction. The energy of the center of mass can be calculated by $K_{cm} = 1/2\mu V^2_{cm}$. The other kinetic energy is that of the U1 and U2, given by $K_1 = 1/2m_1U_1^2$, $K_2 = 1/2m_2U_2^2$, $K'_1 = 1/2m_3U'^2_1$ and $K'_2 = 1/2m_4U'^2_2$. We can calculate the total kinetic energy in the laboratory frame. $K_{1total}= K_1 + K_{cm} = 1/2m_1U_1^2 + 1/2\mu V^2$ and for the products, $K'_{1total} = K'_1 + K_{cm} = 1/2m_3U'^2_1 + 1/2\mu V^2$

It is clear from the above equation that the energy involved in the reaction is from the relative motion of the colliding molecules rather than the overall kinetic energy. It is the relative motion in the cm frame that determines the value of the velocity vectors after the collision. Therefore when examining a hard sphere elastic collisions it is important that relative kinetic energy in the cm frame is conserved and you have $1/2m_1U_1^2 + 1/2m_2U_2^2 = 1/2m_1U'^2_1 + 1/2m_2U'^2_2$.

This means that the law of conservation of energy fixes the final position of the particle 1 after scattering. To describe the collision of atoms and molecules

the conservation of energy must include all the internal excitations of the atoms and molecules. Another energy term that must be included in the conservation of energy associated with the angular momentum. In reactive scattering, the radius of the maximum velocity circle that the products lie on changes depending on the nature of the reaction. Polyatomic systems have internal energy modes that can store energy and therefore the translational energy of the products is not conserved. Fortunately in the center of mass frame, even for reactive scattering, the conservation of momentum applies. The conservation of momentum is used to calculate the momentum and thus the kinetic energy of the undetected product.

The angular distribution of products also changes for reactive scattering. Unlike the scattering of hard spheres, not every collision leads to reaction; you have selective regions for reaction, and therefore you have anisotropic angular distribution.

1.4 DC slice velocity map imaging

After the reactants collide, the resulting product particles velocity vectors change. The technique used here to Image the velocity of the particles is based on ion imaging, which was developed by Chandler and Houston.[7] Using ion imaging they studied the photodisociation dynamics of CH_3I, methyl iodide. The main limitation of the ion imaging technique was the large interaction region compared to the size of the micro-channel diameter on the MCP. This produced blurring, because products with the same velocity created at different points of the reaction region (which is on the order of $6mm^3$) arrived at different parts of the screen.

A decade later a new technique developed by Eppink and Parker,[8] termed velocity map imaging, overcame this problem with ion lenses. The ion lens focuses the ions with the same velocity to the same position on the MCP detector no mater where they were made in the interaction region. This provided much more resolution in the images produced. The problem that remained was that the 3D newton sphere created in the reaction region is projected on to a 2D detector. The 3D image has to be mathematically reconstructed using an inverse able transformation or equivalent mathematical procedure. Then the center slice is taken which contains the relevant information. The inverse able transformation adds noise to the images and also restricts the systems that can be examined to only those with cylindrical symmetry parallel to the imaging plane. Townsend et al.[9] used multiple ion lenses to overcome this problem. In this approach the

expanding ion cloud is not only focused but is stretched along the time of flight direction enough that the MCP could be gated to catch only a central slice of the image. This eliminates the need to reconstruct the image. This technique allows the study of reactions with out any of the previous symmetry restrictions. The dc slice set up is shown in figure 4 and is described more in the experimental section. The images collected from the dc slice imaging setup cannot be analyzed directly, but must be treated. First the background subtraction, that is performed by subtracting the signal intensity from the image generated with the 193nm photodociation laser off. Next the density to flux correction is performed. The density to flux correction is performed because in our experimental setup, our laser determines the number density of products at a given time. During that time the slow particles with velocities close to zero will accumulate in the ionization region and will have a high density, this density is reflected as strong signal intensity. While the fast moving fragments are continuously being removed from the ionization region and have a smaller density. The correction takes this into account and we scale the intensity at each point by the factor $1/(\alpha+v)$ where v is the LAB velocity of the product and alpha is a simple correction factor introduced because the interaction volume and laser pulse width are finite: otherwise a singularity would occur at the LAB origin (v=0).

The resolution of the images is improved further by megapixel ion imaging developed in this lab.[10] This involves a real time calculation of the center of mass for each ion before recording the image. The treatment involves a program called

vision library, developed by Lab View. This program interpolates each pixel to achieve a resolution of up to 0.1 pixels.

1.5 The Cl + Alkane Reaction

The abstraction of hydrogen by a free radical species from a saturated hydrocarbon is an important elementary step in many macroscopic reactions. This elementary reaction plays an important part in the chemistry of the atmosphere of our planet earth, particularly the chemistry of combustion. The interest in studying the chlorine, butane system is that the reaction energetics, reaction barrier and time scale of reaction are ideal for our detection setup. The data gathered provides valuable information about systems that cannot be experimentally determined using macroscopic techniques. Initially crossed beam studies were conducted on tri-atomic systems such as Cl+H2,[11-13] O+H2,[14-16] H+H2,[17-20] and F+H2.[21-23] These reactions are small enough to calculate a complete *ab* initio potential energy surfaces,[24,25] and perform quantum scattering calculations. [26,27] Results from theoretical and experimental data by Andresen and Luntz, [28] using a crossed beam experiment and laser induced florescence (LIF) detection, on the reaction of O (3P) with saturated hydrocarbons, showed that the OH produced was sometimes vibrationally excited but rotationally cold, and the vibrational excitation increased in the order primary-secondary-tertiary abstraction site. A study using diode laser absorption, measured the same low rotational state in the HCl, product. [29] The conclusion is that, the transition state of this reaction is a tight, with linear geometry between the reactants. Also a study by Zare and coworkers[30] using Photoloc, showed the production of cold rotational HCl product. More importantly they showed that the HCl product is

back scattered with respect to the Cl relative velocity vector. The conclusion to the reaction between a radical and saturated ground state hydrocarbon is that only collisions that happen at a small impact parameter will lead to reaction. The smaller the impact parameter, the higher the velocity vector of the reacting molecules along the reaction coordinates. Therefore a reaction between ground state alkanes and radicals like O(3P) and Cl(3P) are said to proceed via a direct reaction. An interesting change can be seen in the imaged HCl product distribution, when the Alkane is excited vibrationally. Selectively exciting the V_3=1 vibrational mode on the hydrocarbon, causes a sharp drop in the backscattered product. Where they only accounts for 30% of the total reaction products. The other 70% is produced in a forward scattered vibrationally cold and rotational excited state. This was explained by the larger reactive cross section of the vibrationally excited molecule. This type of mechanism is called a striping mechanism and it is where the CH_3 product acts as a spectator during the reaction. Varley and Dagdigian [31,32] examined the difference between the reactivity of primary, secondary and tertiary Hydrogen from hydrocarbons. The study was conducted using a technique similar to photoloc and partially deuterated hydrocarbons; they found that the hydrogen abstraction of a primary hydrogen is less dynamically favorable than the abstraction from a secondary or tertiary.

CHAPTER 2 - EXPERIMENTAL SECTION

2.1 The Molecular Beams

The experiment was conducted on a crossed beam device that is described in more detail elsewhere. [33-48] Briefly explained here, the molecular beams are generated by the supersonic expansion of a gas through a small opening, by the differential pumping of the main chamber through the source chamber. Both beams start by seeding a precursor of the reactant in a noble gas that will control the translational energy of the reactants. We made mixtures of fixed concentrations. The butane beam is skimmed once before entering the reaction main chamber. The Cl beam is generated by passing helium over a bubbler containing oxalyl chloride $(COCl)_{2,}$ which is held at 0C°. The oxalyl chloride beam is photo-dissociated, to form Cl radicals, using the 193nm output from an ArF excimer laser (60mj, 10 Hz). The laser is loosely focused, using a 35cm MgF_2 lens, on the tip the piezoelectric pulsed valve. Oxalyl chloride has a large absorption cross section at 193nm, and each oxalyl chloride molecule produces 2 Cl radicals. Both of which are entrained in and create an intense Cl radical beam. The chlorine radicals are produced in two spin-orbit states, $^2P_{3/2}$ and $^2P_{1/2.}$ Where the $^2P_{1/2}$ is 882cm^{-1} higher in energy than the $^2P_{3/2}$ state.[49-50] The excited Cl radicals produced are quenched into the lower energy state, before entering the reaction chamber. Both beams are sent through the source

chambers so that they meet at 90 degrees in the main chamber. The spread in velocity for the reactant beams was 8% at FWHM. The pressure in the main chamber was held at 10^{-8} resting pressure and 10^{-6} operating pressure. Figure 6, below shows how the $(COCl)_2$ is photo-dissociated with the 193nm laser.

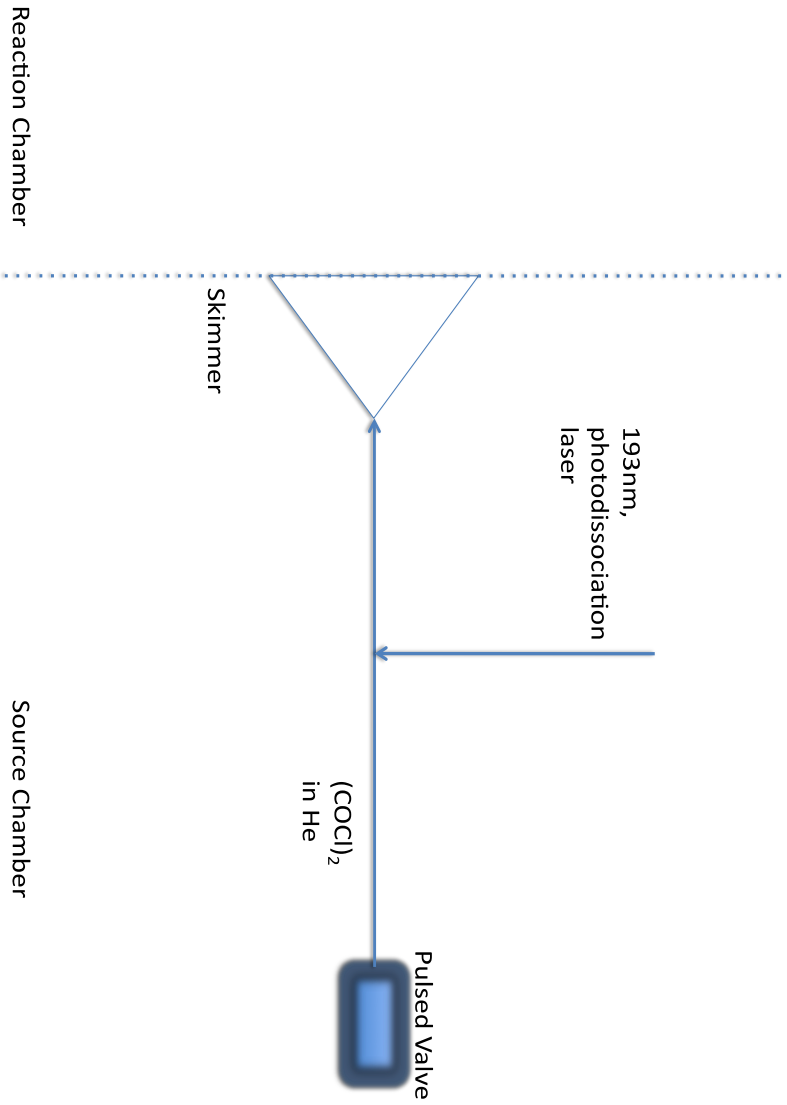

Figure 6 Schematic of Cl beam created by the photodissociation of $(COCl)_2$ using a 193nm laser

2.2 Vacuum Chamber

Velocity map imaging must be carried out under single collision parameters, in order to preserve the angular and translational energy distributions after the reactive scattering. The only way to achieve single collision conditions is to ensure a large enough free path for the reactants and products. The large mean free path is created, by evacuating the reaction chamber to a pressure of 10^{-6} torr.

The crossed beam machine we are using was first called the “Universal Imaging Machine” and is described in earlier publication in more detail.[9] The main chamber has 12” conflat cross openings on each face of the cubic center chamber. The main chamber also has 4 x 2.75” conflat ports at 45° to the main ports in the horizontal plane. The conflat openings along the vertical axis are used for the turbo pump and the TOF tube and detector. Two of the 12” ports, opposite each other are bolted up. The other two openings connect the main chamber to the two source chambers. The source chambers are connected to the main chamber only through a 1mm skimmer. The source chambers and the main chamber are differentially pumped using molecular turbo pumps (Osaka). A single, Welch 1397 oil roughing, pump takes the exhaust of all three pumps away. The source chambers are fitted with mounts that hold the piezo electric pulsed values. The tips of the nozzles are held 4cm away from the skimmer.

2.3 Direct current slice imaging and data analysis.

The created radical products resulting from H abstraction with m/z=83, were ionized by single photon ionization, using a 157 nm F_2 excimer laser (OPTEX, 0.5 mJ, 10 Hz) focused loosely with a MgF_2 lens (f = 135 cm) into the reaction region. A dc slice imaging detection method coupled with the megapixel acquisition program IMACQ produced the images presented here. The dc slice imaging setup is described in previous publications of this lab and a schematic is shown.[51] Briefly, the setup consists of three ion lenses and a repeller. Resistors were placed between the ion optics to create a more stable and homogeneous electrostatic field. After ionization of the product molecules, the potential difference between the repeller and the first ion lens accelerates the molecules out of the interaction region. The second ion lens is used to focus ions with the same velocity to the same spot on the MCP detector regardless of where in the reaction region they where created. This gives sharp images without the blurring caused by the large area of the reaction region compared to the pixel size. The third ion lens is used to stretch the arrival time (Δt) of the ion sphere so that Δt is large enough to be gated, 40ns in our experiment. This is what allows us to collect the center slice of the ion sphere without needing to do any mathematical reconstruction. After passing through the ion lens 3, the ions enter a field free time of flight region that leads to the detector. The distance between the interaction region and the detector is 105cm.

The detector is made up of a pair of 80mm diameter micro channel plates

(MCP), coupled to a P47 phosphor screen held at 6KV (Burle Electro-Optics). The front of the MCP is held at ground and the back is gated for ions with a specific mass by applying a high voltage pulse using a commercial pulsar (DEI PVX-4140, Fort Collins, CO). The voltage applied to the MCP is 2.5KV with a 1KV bias. The timing of the gate of the MCP pulse with respect to the molecular beams and the firing both the 193nm photo dissociation laser and the 157nm probe laser are controlled by a commercial delay generator (BNC 555, San Rafael, CA). The images are produced by the bombardment of the ions, on the MCP assembly, are captured by a charge coupled device camera (Mintron 2821e, 512, 480 pixels, Taipei, Taiwan). The image is than sent to the computer, where the dc slice imaging detection scheme, centroiding and megapixel acquisition program IMACQ were used to accumulate the raw images.

The image accumulation required to reach a good signal to noise ratio took 1-3h for each collision energy. Additionally the images of the scattering with the 193nm laser off, essentially the elastic scattering of $(COCl)_2$ with butane is also collected for background subtraction from the raw images. From previous studies the major contributor to the background was the photodissociation of the parent hydrocarbon; this photodissociation occurred in the vicinity of the hydrocarbon beam and made the signal in that area of the image unreliable. By using a higher intensity beam of Cl and lowering the focusing setup for the probe laser, we reduced the background intensity compared to the signal intensity. This makes it possible to extrapolate the results of scattering in the forward direction,

which show some remarkable aspects of the dynamics of the reaction.

CHAPTER 3 - RESULTS

The most powerful aspect of dc slice imaging, as applied to crossed beam reactive scattering experiments, is to display in a single image the full coupling of the translational and angular distributions and the location of the center of mass. Previous techniques only elucidate the center of mass and use strategic methods, not based usually on the collected data, to fit the data. Using this technique, we studied the H abstraction reaction, $Cl + C_4H_{10} \rightarrow HCl + C_4H_9$ at two collision energies, 6.5 and 9.0 kcal/mol.

The collected data will first go through a background subtraction, and then must be corrected using a density to flux correction. This correction takes into account that the slower fragments spend more time in the ionization region than the faster fragments. Therefore slower fragments accumulate in the ionization region from collisions that take place before the probe laser is fired. The correction is easily applied by scaling each pixel intensity by the factor $1/(\alpha+\nu)$, where ν is the laboratory velocity of the fragment. α Is an empirically determined parameter that accounts for the finite size of the reaction volume and prevents the signal from approaching infinity at low velocity.[52]

An issue that must be addressed is the difference in the ionization energy of the two products from the reaction. The primary radical has higher ionization energy than the secondary radicals; this means that the intensity of our signal will be composed of more 2-butyl radicals. This issue has been addressed before in

this lab. The study compared the relative ionization efficiency for several heptane isomers, using a 157 nm laser.[53] Results showed little variation, less than 20%, in detection efficiency for the various isomeric radical products of heptane. This small variation will allow us to not consider this difference, and we will thus neglect this deviation in the current study.

Figure 7 shows the dc sliced images of the butyl radical products, for both collision energies after background subtraction and density-to-flux correction. A newton diagram is superimposed on the images for reference.

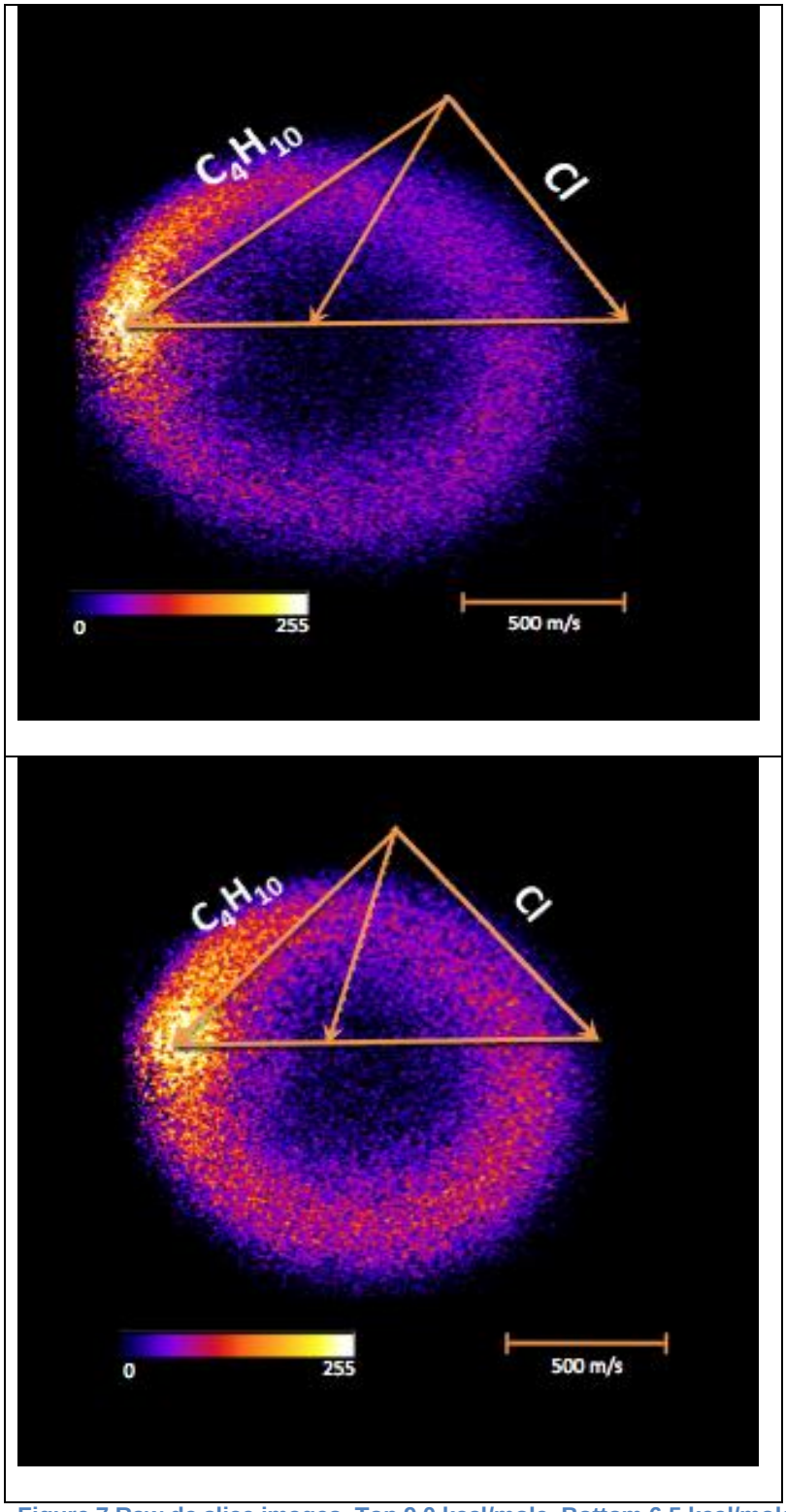

Figure 7 Raw dc slice images. Top 9.0 kcal/mole. Bottom 6.5 kcal/mole.

Figure 8 shows the total translational energy distributions, integrated over all angles. This shows that the translational energy distribution for the 6.5 kcal/mole collision energy peaks at 5.0 kcal/mole and for the 9.0 kcal/mole collision energy the translational distribution peaks at 7.5 kcal/mol. At a translational energy of 12.5, the 6.5 and 9.0 kcal/mole distributions overlap and extend out to beyond 20 kcal/mol. Overall both distributions are very similar.

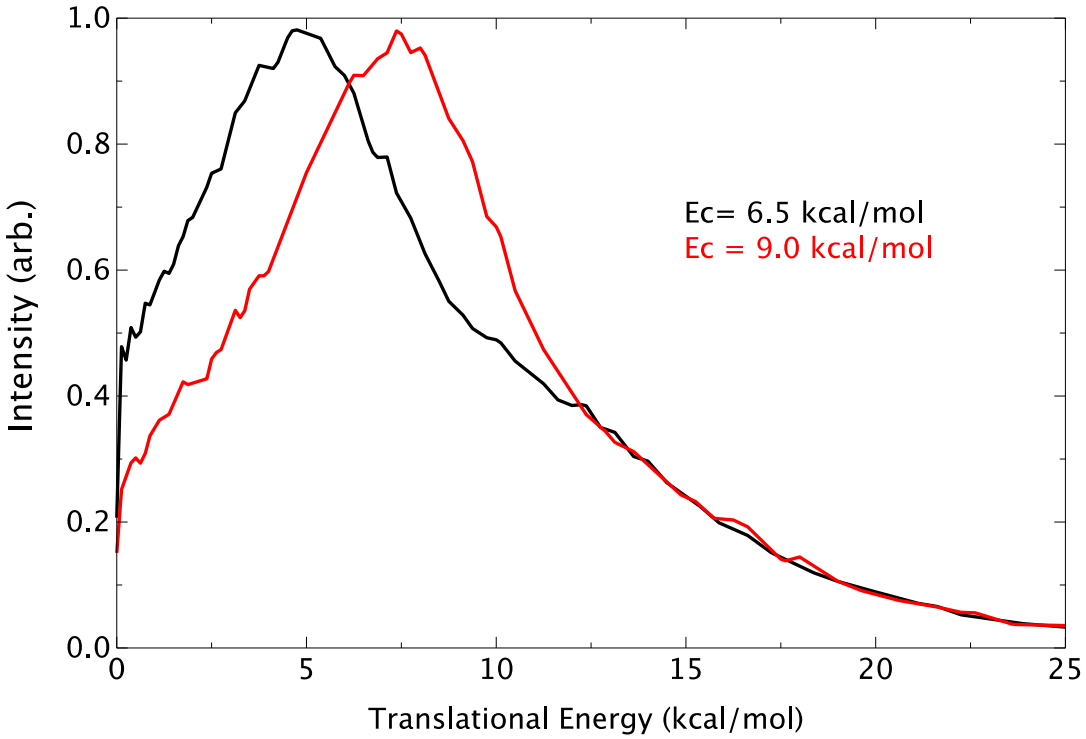

Figure 8 Total translational energy distributions, integrated over all angles.

The center of mass angular distribution shown in Figure 9 is integrated over all recoil velocities. At 6.5 kcal/mole collision energy the distribution has slightly higher signal intensity in the backward direction. At the 9.0 kcal/mole collision energy, there are more products collected in the forward direction with an equal decrease in the backscattered intensity. Overall both angular distributions looked very similar and show forward backward symmetric scattering, which indicates that there is at least two different mechanisms involved.

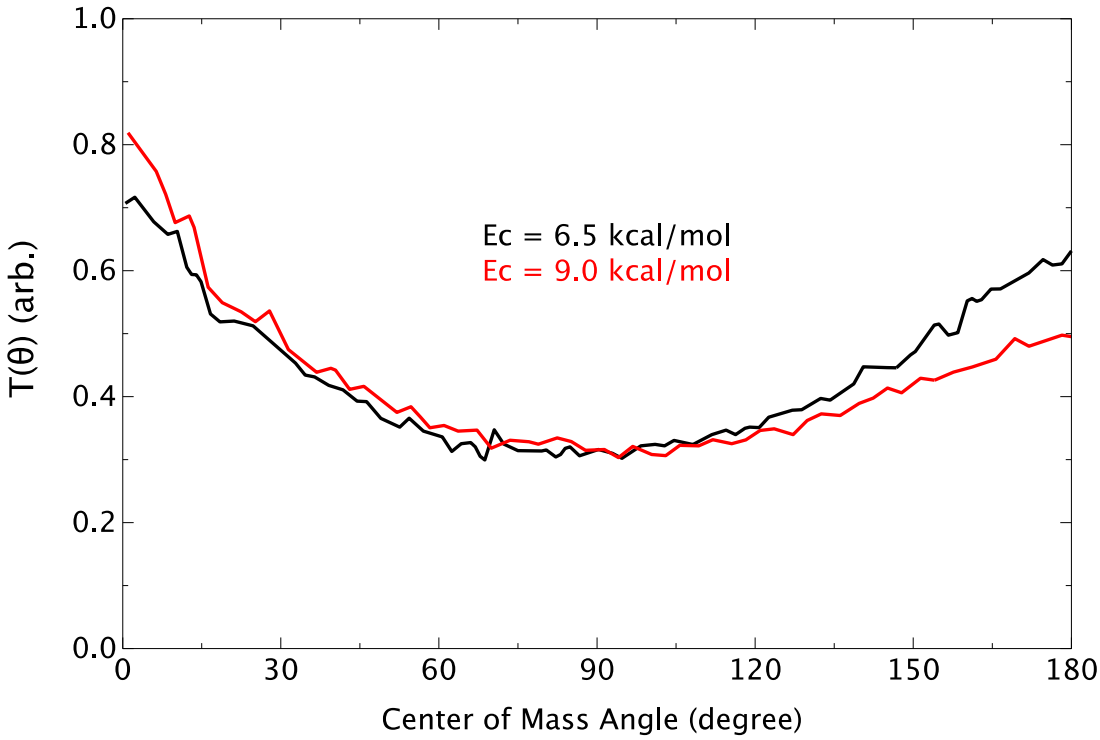

Figure 9 Center of mass angular distributions, integrated over all recoil velocity.

To further examine the coupling between the translational and angular distribution, we divided the images into three sectors the forward 0-60°, sideways 60-120°, and backward 120-180° each individually normalized. These are shown in Figure 10-Figure 12 below. The forward scattering shows the strongest dependence on collision energy while the side scattered product show less dependence on collision energy. The back-scattered product shows the least dependence on the collision energy.

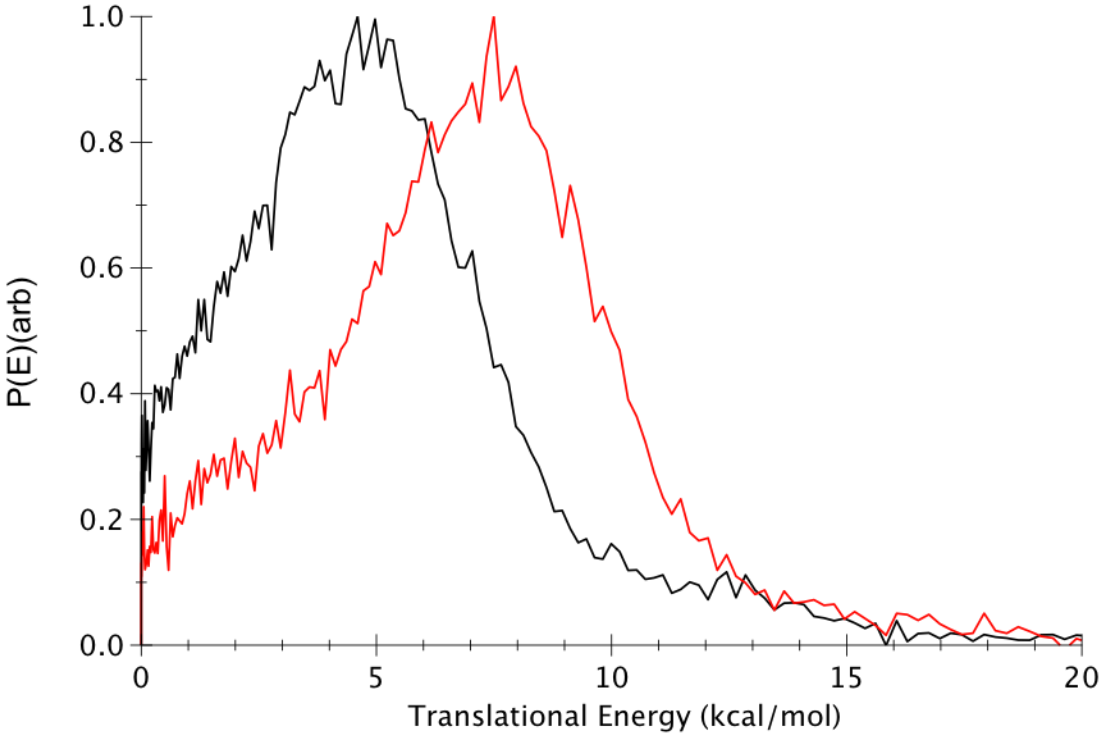

Figure 10 Forward distribution (0-60) red 9.0kcal/mole and black 6.5kcal/mole.

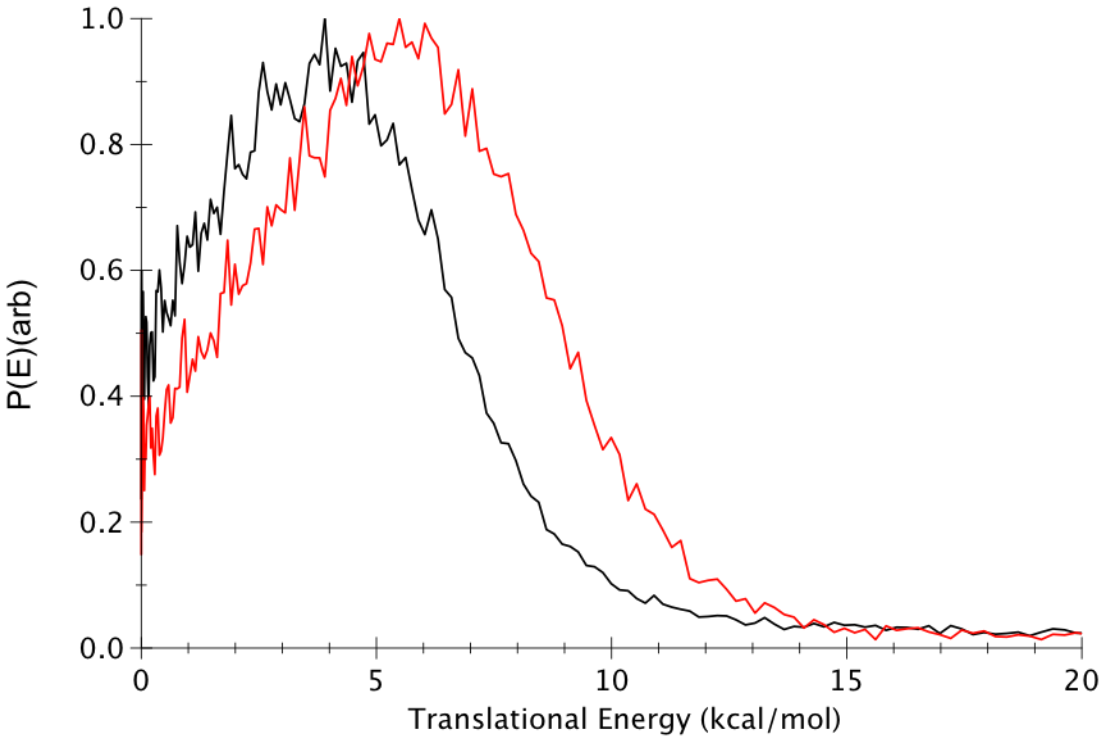

Figure 11 Sideways distribution (60-120) red 9.0 kcal/mole black 6.5kcal/mole.

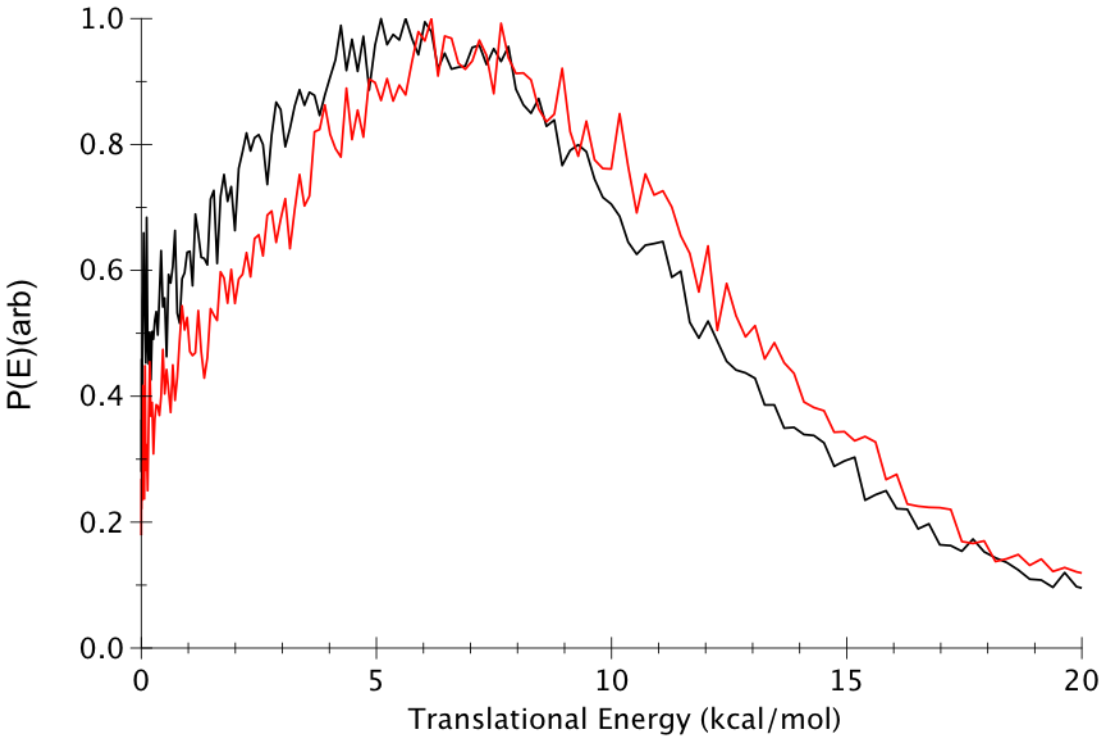

Figure 12 Backward distribution (120-180) red 9.0kcal/mole and black 6.5kcal/mole

CHAPTER 4 - DISCUSSION

4.1 Discussion

We start by examining the translational energy distributions shown in Figure 8. This shows that the translational energy distributions at both collision energies are very similar. The most obvious difference is that the higher collision energy peaks at a higher translational energy. The distributions also show that the collision energy is strongly coupled into the translational energy of the products. This behavior is typical for a collinear heavy-light-heavy (HLH) system, such as the one we are examining. Plotted in Figure 13 is the scaled translational energy distribution, which gives a better understanding of the energy disposition during the scattering particularly for a HLH system. For the 9.0 kcal/mole collision energy, it can be seen that 60% of the products have a translational energy less than or equal to the collision energy. At the 6.5 kcal/mole collision energy, approximately 80% of products have translational energy greater than the collision energy. These results are expected because the exoergicity, averaged for the two sites is 4 kcal/mole. Some of the exoergicity is transformed into translational energy, and the remainder is converted to rotational and vibrational excitations in the product molecules. Previous studies have shown that the distribution preserves the collision energy into product recoil.[54, 55]

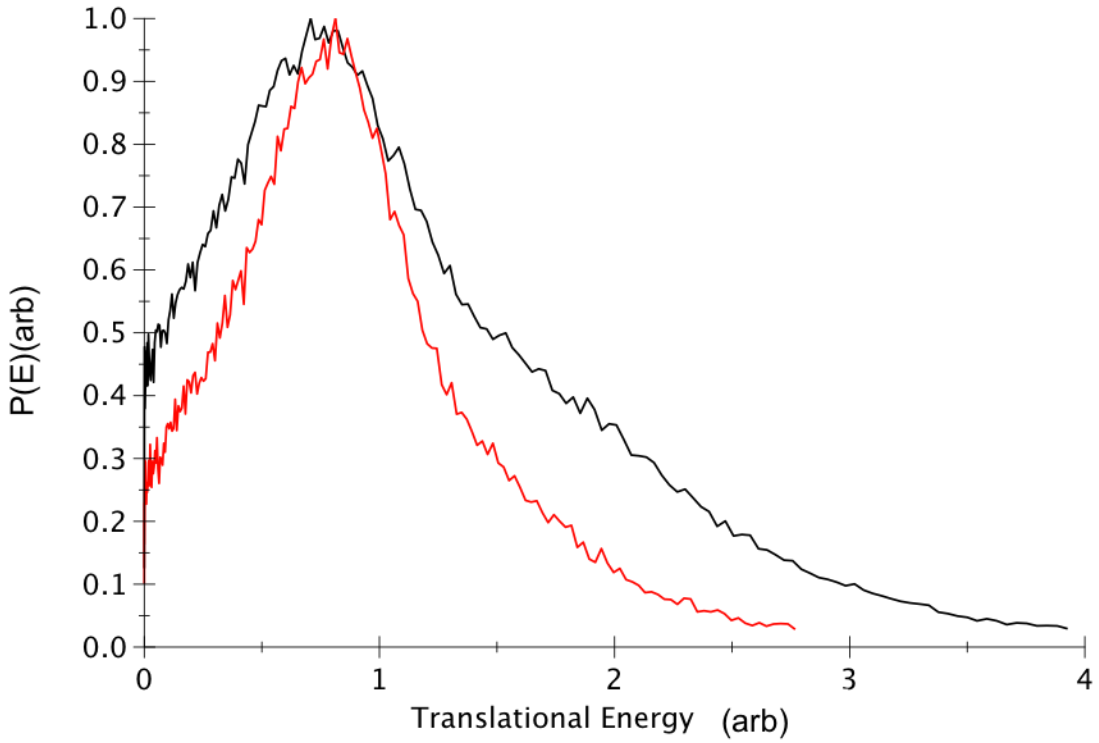

Figure 13 Reduced translational energy distribution integrated over all scattering angles, red 9.0 kcal/mole, and black 6.5kcal/mole.

To calculate the available energy for this reaction we must take into consideration the difference between the extractions of a primary or secondary hydrogen. Each extraction leads to different values of available energy. If we take the average exoergicity for primary and secondary hydrogen as 4 kcal/mole, and we further assume that all reaction sites equally probable. This gives an available energy of 10.5 and 13 kcal/mole for the 6.5 and 9.0 kcal/mole collision energies respectively. We then find the fraction of available energy appearing in translation as 0.48, with forward, sideways, and backscattered contributions

calculated as 0.48, 0.38, and 0.57, for the low collision energy. At he high collision energy we found 0.58, 0.58, 0.42, and 0.54 for the total, forward, sideways, and backscattered contributions respectively. These results are lower than the 0.68 reported by Bass et al.[52] for n-butane.

Table 1 Average system energy, E_c collision energy, and $<E_T>$ Average translational energy, $<E_T>^*$ Average reduced translational energy in kcal/mole.

E_c	$<E_T>_{total}$	$<E_T>_{forward}$	$<E_T>_{sideways}$	$<E_T>_{back}$	$<E_T>^*_{total}$	$<E_T>^*_{forward}$	$<E_T>^*_{sideways}$	$<E_T>^*_{back}$
6.5	5.0	4.5	4.0	6.0	0.77	0.90	0.61	1.2
9.0	7.5	7.5	5.5	7.0	0.83	0.85	0.61	0.6

A better indicator of the coupling in the energy of this reaction is the angle-dependent scaled translational energy distributions, shown in Figure 14-Figure 16. By dividing the scattering into different regions forward, sideways and backward we can see more features of the energy distribution. The forward scattered product peaks at 0.85 E_c and 0.90 E_c for low and high collision energy respectively. Forward scattering is expected for a spectator striping mechanism. This happens when the product has similar momentum before and after the reaction. For the case of hydrogen abstraction by a chlorine the average expected translational energy is $E_T = E_c\,(35/36)^2 = 0.95\,E_c$, the values we report are consistent with this. This suggests that with the striping mechanism the collision energy is strongly coupled into the translation and the reaction exoergicity is coupled into the internal degrees of freedom of the products. The

side scattered product distribution, shows little dependence on collision energy. At both collision energies the side-scattered product had the lowest average fractional translational energy with 0.8 and 0.4 kcal/mole for the low and high collision energies respectively. This is attributed to an intermediate impact parameter were there is rotational excitation of the butyl radical but no coupling of the exoergicity into the recoil. For the back-scattered product low collision energy both have a broad distribution with an average scaled translational energy at high collision energy was $0.6E_c$, and at the lower collision energy it was $1.2\ E_c$. This result is to be expected because of the little difference in the translational energy of the back-scattered product at both collision energies as shown in Figure 12. Because of the weak dependence on collision energy in the backscattering the reduced translational energy shows the difference in average reduced translational energy. The $1.2E_c$ suggests a coupling of the reaction exoergicity into the translational energy. Evans et al developed a simple model used to model the backscattered product average energy [57]

$\langle E_T \rangle = E_c \cos^2 \beta + E_R \sin^2 \beta$. Where β is the skew angle for the reaction, in the case of Hydrogen β is equal to 0.96, E_R is the reaction energy and E_c is the collision energy. This model predicts the $\langle E_T \rangle = 0.95$. The deviation in our results from this simple model can be expected. The model was developed to describe collinear low impact parameter collisions or triatomic systems. For the butane system, the reaction exoergicity and the internal degrees of freedom in the reactants are strongly coupled into the backscattered product distribution.

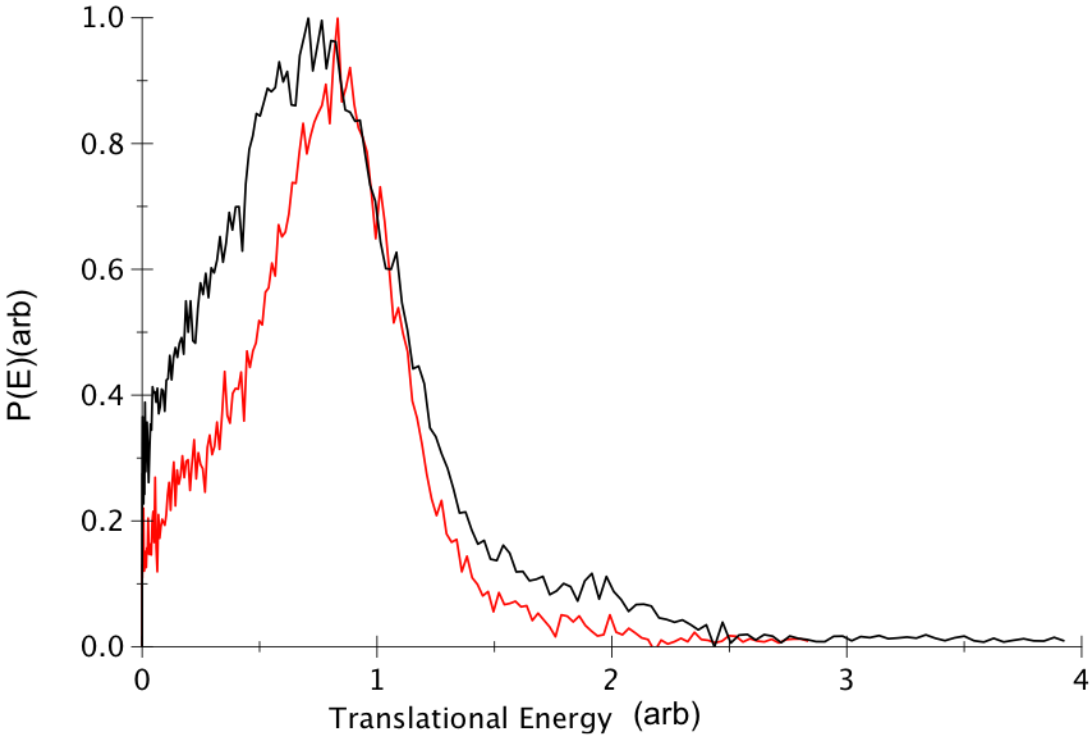

Figure 14 Forward reduced energy distribution (0-60) red 9.0kcal/mole and black 6.5kcal/mole

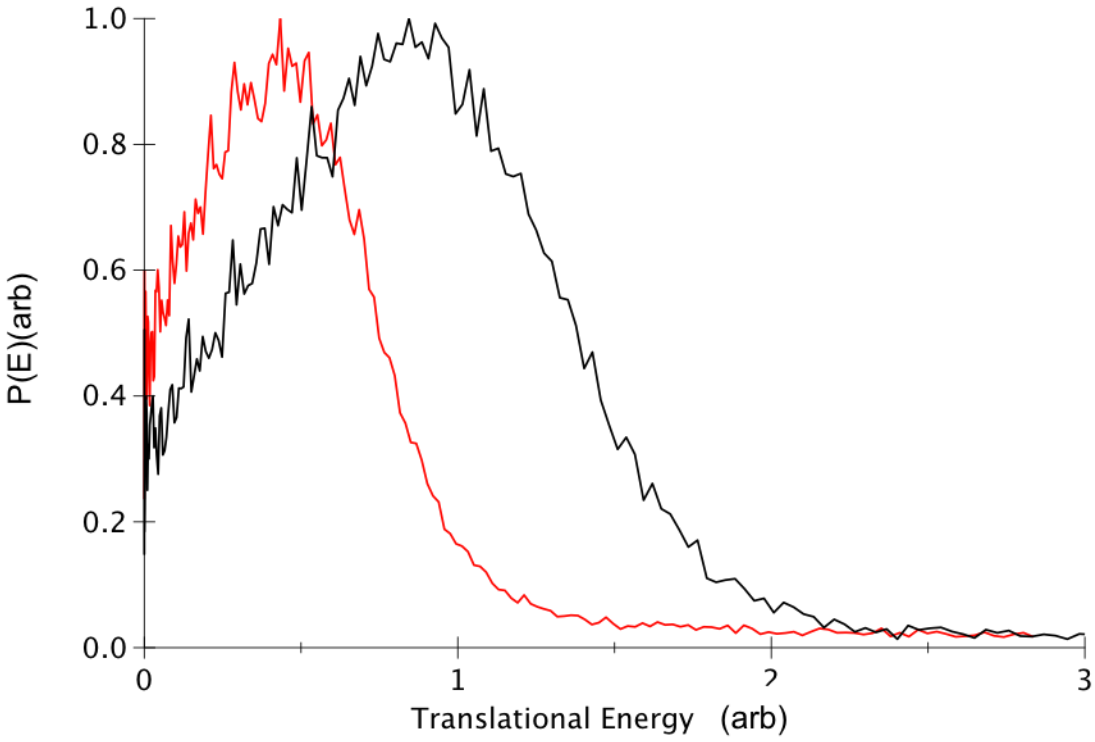

Figure 15 Sideways-reduced translational energy distribution (0-60) red 9.0kcal/mole and black 6.5kcal/mole.

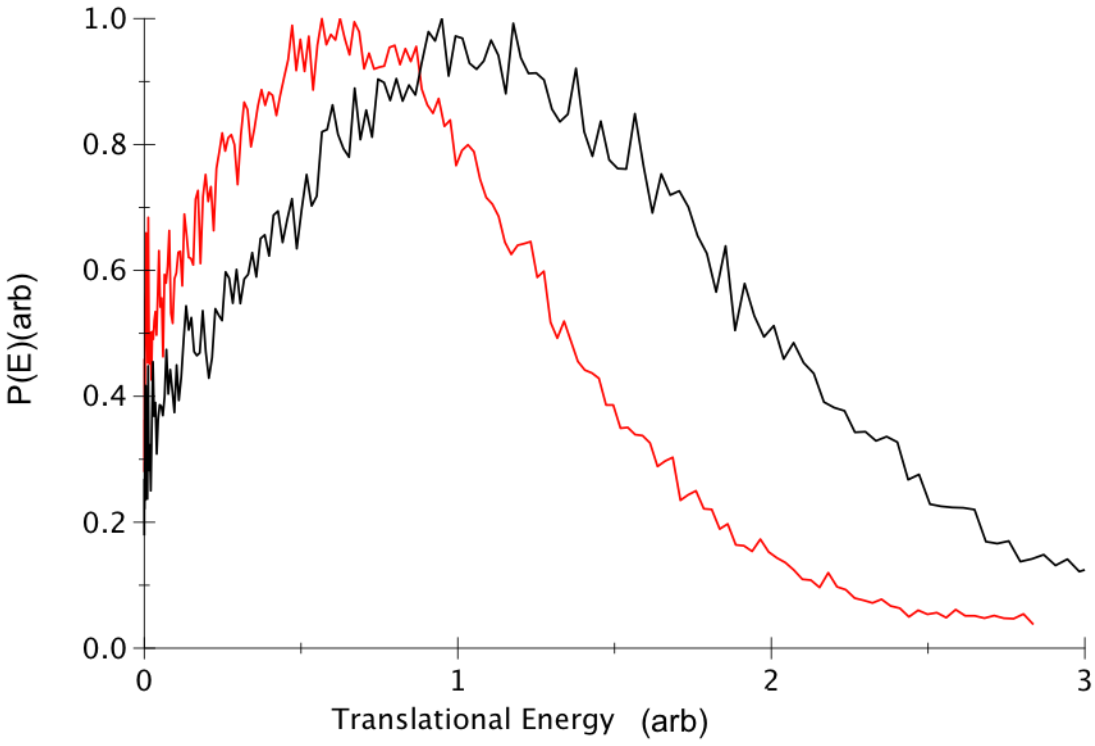

Figure 16 Backward translational energy distribution (0-60) red 9.0kcal/mole and black 6.5kcal/mole.

Many dynamics experiments have been conducted, on the reaction of alkanes with Cl radical. A study by Koplitz and coworkers [58] examined the relative reactivity of partially deuterated propane, butane, and isobutene. Assuming a single recoil energy and that the hydrocarbon has no internal energy, they showed enhanced scattering, for the HCl in the back scattered direction for the reaction of Cl + $CD_3CH_2CD_3$, and side scattering was dominated by the DCl. Varley and Dagdigian [59,60] used photoloc to examine the relative reactivity at different sites of alkanes. Both groups argued that the secondary and tertiary sites are more reactive than the primary site. The sensitivity of reaction site decreases with increasing collision energy.

A study by Hemmi and Suits using Cl + n-pentane at high collision energy reported forward scattering, much like the results shown here. They argued that the forward scattering is due to the abstraction of secondary hydrogen and the backscattering is due to the abstraction of a primary H. The conclusion is similar to the one reached by Blank et al. in the case of propane. Using photoloc with ion imaging on the reaction of Cl + n-butane Bass et al,[61] reached the opposite conclusion. Two experiments recently performed in this lab, using the same set up as this experiment, showed that the reaction dynamics at both sites to be similar. The first involved the reaction of Cl + n-pentane, isopentane and neo-pentane; in the second reaction is that of Cl + 1,1,1,4,4,4-d, butane. Both reactions had angular and translational energy distributions that are very similar for the reaction at primary or secondary sites.[54,55]

The angular distributions are also similar; both show nearly forward backward scattering symmetric scattering. This shows that both mechanisms are happening at both energies. The back scattering is stronger for the low collision energy and for the high collision energy the forward scattering becomes more active. As shown in previous studies, our results show that the backscattering contribution is still preferred even at high collision energy. These results are consistent with findings of this lab on previous Cl + alkane reactions and with the Hemmi and Suits' n-pentane reaction. Bass et al, [56] using photoloc imaging experimental configuration showed sharp forward peaking, for the Cl + n-butane reaction. Bass associated this forward signal to the abstraction of a primary

hydrogen. This study is inconclusive because the experiment is not able to detect any backscattered product with translational energy less than the available collision energy because of interference with the HCl in the beam.[62]

Zare and coworkers developed a model that described the reaction of Cl + methane, using a combined line of centers hard spheres. In this model the translational energy vector, normal to the potential barrier determines the probability of crossing. The hard sphere model was used for the angular distribution in this model. This model can also be adjusted by including an opacity function to account for the forward scattering, high impact parameter collisions. This model must further be adjusted for the differences between methane and butane. The most important difference is that the reaction seems to be barrier-less for butane and exothermic; and it is endothermic with a significant reaction barrier for methane. The possibility of there being a submerged reaction barrier was investigated by Greaver et al.[63] With any barrier, the line of centers model shows that enough energy must be along the line of centers to overcome the barrier. Therefore for low impact parameter collisions the reaction is likely. In the case of methane the collinear Cl-H-C collision is a low impact parameter collision. In the case of butane the same collision is necessarily off center. These collinear, off-center collisions lead to a rotational excitation of the butyl radical and a vibrationally excited HCl product. Further examination is needed to investigate the relation between the impact parameter and the rotational excitation in the butyl radical to deduce the rotational levels that can be achieved.

While examining the impact parameter for butane it is important to discuss the conformational isomers of the butane. The two conformational isomers of butane are the anti and gauche confirmation, with the anti conformation being 0.62 kcal/mole lower in energy than the gauche confirmation, with a 3.5 kcal/mole energy barrier.[64] The energy barrier is too high for the molecules to overcome during the supersonic expansion. Which means approximately 25% of the molecules are in the gauche conformation. The cross section for the collision is much larger almost double for anti-conformation; this would lead to a higher probability of a collision with a Cl radical. The gauche conformation has a 0.62 kcal/mole energy level higher than the anti conformation. This energy and collision cross section difference between the anti and gauche conformation and their effect on the reaction need to be further investigated.

4.2 Conclusion

The symmetric back and forward scattering angular distribution shows that the reaction is proceeding via two different pathways. The first is the stripping mechanism in which the butane is acting as a spectator, which is what leads to forward scattered product. The rebound or direct mechanism involves a low impact parameter coupled with a collinear reaction trajectory, which gives the back and side scattered product. The translational energy distribution showed that the forward scattering was the most dependent on the collision energy, while the side scattered distribution showed slight dependence on collision energy. The backscattered products showed weak dependence on collision energy and the distributions for both high and low energy are almost overlapping. The backscattered distributions peak at a higher energy and show some of the reaction exoergicity associated with the translational energy of the product. A clear indication of a near zero impact parameter collision. The two conformational isomers of n-butane, and the change in impact parameter and energy levels associated with them, complicate the analysis of the results. More research needs to be conducted to isolate the correlation between the different impact parameter collisions, the conformational isomers, scattering direction and energy state of the product. Finally at the high collision energies used, all the reaction sites become equally probable and so you lose sensitivity. This means that any subtle differences that exist for different reaction sites, and any reaction barriers associated with them, are not distinguishable at the high E_c. This experiment was

limited by low signal to noise ratio at the lower collision energies. The solution will be to use state selective product detection of the HCl product. This will solve the problem of the high noise level at low collision energies and give a more detailed understanding of the selective energy release for this reaction.

REFERENCES

1 C. M. Guldberg, Concerning the Law of Chemical Affinity, C. M. Forhandlinger Videnskabs-Selskabet Christina (1864).

2 Arrhenius, S. Z. Phys. Chem. (Leipzig) 1889, 4, 226. van't Hoff, J. H. In Etudes de Dynamiques Chimiques; F. Muller and Co.: Amsterdam, 1884; p 114 (translation by T. Ewan, London, (1896).

3 D. R. Herschbach, Molecular Dynamics of Elementary reactions, Noble Lecture. 8 December 1986.

4 G. M. Hendrick L. Bethlem, International reviews in physical chemistry. 2003, 22 (1), 73.

5 R. D. Levine, Molecular reaction dynamics. (Cambridge University Press, New York (2005).

6 Henriksen, N. Theories of molecular reaction dynamics: the microscopic foundation of chemical kinetics; Oxford University Press, 2008.

7 D. W. Chandler and P. L. Houston, J. Chem. Phys. 1987, 87, 1445.

8 A. Eppink and D. H. Parker, Rev. Sci. Instrum. 1997, 68, 3477.

9 D. Townsend, M. P. Minitti, and A. G. Suits, Rev. Sci. Instrum. 2003, 74, 2530.

10 L. Wen, D. C. Steven, A. L. Sridhar and G. S. Arthur, Review of scientific interments, 2005, 76 (6), 063106.

11 M. Alagia, N. Balucani, L. Cartechini, P. Casavecchia, E. H. van Kleef, G. G. Volpi, F. J. Aoiz, L. Banares, D. W. Schwenke, T. C. Allison, S. L. Mielke, and D. G. Truhlar, Science, 1996, 273, 1519.

12 S. H. Lee and K. P. Liu, J. Chem. Phys. 1999, 111, 6253.

13 F. Dong, S. H. Lee, and K. Liu, J. Chem. Phys. 2001, 115, 1197.

14 M. Ahmed, D. S. Peterka, and A. G. Suits, Chem. Phys. Lett. 1999, 301, 372.

15 D. C. Che and K. P. Liu, J. Chem. Phys. 1995, 103, 5164.

16 Y. T. Hsu, K. Liu, L. A. Pederson, and G. C. Schatz, J. Chem. Phys. 1999, 111, 7921.

17 R. E. Continetti, B. A. Balko, and Y. T. Lee, J. Chem. Phys. 1990, 93, 5719.

18 L. Schnieder, K. Seekamp-Rahn, J. Borkowski, E. Wrede, K. H. Welge, F. J. Aoiz, L. Banares, M. J. Dmello, V. J. Herrero, V. S. Rabanos, and R. E. Wyatt, Science. 1995, 269, 207.

19 L. Schnieder, K. Seekamp-Rahn, E. Wrede, and K. H. Welge, J. Chem. Phys. 1997, 107, 6175.

20 T. N. Kitsopoulos, M. A. Buntine, D. P. Baldwin, R. N. Zare, and D. W. Chandler, Science, 1993, 260, 1605.

21 F. J. Aoiz, L. Banares, V. J. Herrero, V. S. Rabanos, K. Stark, and H. J. Werner, Chem. Phys. Lett. 1994, 223, 215.

22 D. M. Neumark, A. M. Wodtke, G. N. Robinson, C. C. Hayden, and Y. T. Lee, Phys. Rev. Lett. 1984, 53, 226.

23 D. M. Neumark, A. M. Wodtke, G. N. Robinson, C. C. Hayden, and Y. T. Lee, J. Chem. Phys. 1985, 82, 3045.

24 F. J. Aoiz, L. Banares, J. F. Castillo, B. Martinez-Haya, and M. P. de Miranda, J. Chem. Phys. 2001, 114, 8328.

25 P. A. Whitlock, J. T. Muckerman, and E. R. Fisher, J. Chem. Phys. 1982, 76, 4468.

26 S. D. Chao, S. A. Harich, D. X. Dai, C. C. Wang, X. M. Yang, and R. T. Skodje, J. Chem. Phys. 2002, 117, 8341.

27 D. X. Dai, C. C. Wang, S. A. Harich, X. Y. Wang, X. M. Yang, S. D. Chao, and R. T. Skodje, Science. 2003, 300, 1730.

28 A. C. Luntz and P. Andresen, J. Chem. Phys. 1980, 72, 5851.

29 J. H. Park, Y. S. Lee, J. F. Hershberger, J.M. Hossenlopp and G. W. Flynn, J. Am. Chem. Soc. 1992, 114, 58.

30 W. R. Simpson, A. J. Orrewing and R. N. Zare, Chem. Phys Lett. 1993, 212,163.

31 D. F. Varley and P. J. Dagdigian, Chem. Phys. Lett., 1996, 255,393.

32 D. F. Varley and P. J. Dagdigian, J. Phys. Chem. 1996, 100, 4365.

33 C. S. Huang, W. Li, and A. G. Suits, J.Chem. Phys. 2006, 125, 133107.

34 D. W. Chandler and P. L. Houston, J. Chem. Phys. 1987, 87, 1445.

35 A. Eppink and D. H. Parker, Rev. Sci. Instrum. 1997, 68, 3477.

36 J. J. Lin, J .G. Zhou, W. C. Shiu, and K. P. Liu, Science. 2003, 300, 966.

37 W. Shiu, J. J. Lin, K. P. Liu, M. Wu, and D. H. Parker, J. Chem. Phys. 2004, 120, 11.

38 J. G. Zhou, W. C. Shiu, J. J. Lin, and K. P. Liu, J. Chem. Phys. 2004, 120, 5863.

39 J. G. Zhou, W. C. Shiu, J. J. Lin, and K. P. Liu, J. Chem. Phys. 2006, 124, 104309.

40 D. A. Blank, N. Hemmi, A. G. Suits, and Y. T. Lee, Chem. Phys. 1998, 231, 261.

41 N. Hemmi and A. G. Suits, J. Chem. Phys. 1998, 109, 5338.

42 H. U. Stauffer, R. Z. Hinrichs, P. A. Willis and , H. F. Davis, J. Chem. Phys. 1999, 111, 4101.

43 P. A. Willis, H. U. Stauffer, R. Z. Hinrichs, and H. F. Davis, J. Chem. Phys. 1998, 108, 2665.

44 R. L. Gross, X. H. Liu, and A. G. Suits, Chem. Phys. Lett. 2003, 376, 710.

45 X. H. Liu, R. L. Gross, G. E. Hall, J. T. Muckerman, and A. G. Suits, J. Chem. Phys. 2002, 117, 7947.

46 X. H. Liu, R. L. Gross, and A. G. Suits, J. Chem. Phys. 2002, 116, 5341.

47 M. Ahmed, D. S Peterka, and A. G. Suits, Chem. Phys. Lett. 2000, 317,264.

48 M. Ahmed, D. S. Peterka, and A. G. Suits, Phys. Chem. Chem. Phys. 2000, 861.

49 Y. Ralchenko, A. E. Kramida, J. Reader, and NIST ASD Team, NIST Atomic spectra Satabase (version 3.1.5), 2008, available at http://physics.nist.gov/asd3 (11 March 2012).

50 M. Ahmed, D. Blunt, D. Chen, A. G. Suits, J. Chem. Phys. 1997, 106, 7617.

51 W. Li, S. D. Chambreau, S. A. Lahankar and A. G. Suits, Rev. Sci. Instrum. 2005, 76, 63106.

52 W. Li, C. Huang, M Patel, D. Wilson, and A. Suits, J. Chem. Phys. 2006, 124, 011102.

53 R. Silva, W. K. Gichuhi, M. B. Doyle, A. H. Winney, and A. G. Suits, Phys. Chem. Chem. Phys. 2009, 11, 4777.

54 A. D. Estillore, L. M. Visger, T. A. Ghani and A. G. Suits, Phys. Chem. Chem. Phys. 2011, 13, 8433-8440.

55 A. D. Estillore, L. M. Visger, and A. G. Suits, J. Chem. Phys.2010, 132, 164313.

56 M. J. Bass, M. Brouard, C. Vallance, T. N. Kitsopoulos, P. C. Samartzis, and R. L. Toomes, J. Chem. Phys. 2004, 121, 7175.

57 G. T. Evans, E. van Kleef and S. Stolte, J. Chem. Phys. 1990, 93, 4874.

58 Y.F. Yen, Z. R. Wang, B. Xue, and B. Koplitz, J. Phys. Chem. 1994, 98, 4.

59 D. F. Varley and P. J. Dagdigian, Chem. Phys. Lett. 1996, 255, 393.

60 D. F. Varley and P. J. Dagdigian, J. Phys. Chem. 1996, 100, 4365.

61 M. J. Bass, M. Brouard, C. Vallance, T. N. Kitsopoulos, P. C. Samartzis, and R. L. Toomes, J. Chem. Phys. 2004, 121, 7175.

62 M. J. Bass, M. Brouard, C. Vallance, T. N. Kitsopoulos, P. C. Samartzis, and R. L. Toomes, J. Chem. Phys. 2003, 119, 7168.

63 S. J. Greaves, A. J. Orr-Ewing, and D. Troya, J. Phys. Chem. 2008, 112, 9387.

64 N. L. Allinger, J. T. Fermann, W. D. Allen and H. F. Schafer, J. Chem. Phys. 1997, 106, 5143.

ABSTRACT

DC SLICE IMAGING, CROSSED BEAM REACTION OF CHLORINE RADICAL WITH BUTANE

by

TAREK ABDUL GHANI

December 2012

Advisor: Dr. Arthur Suits

Major: Chemistry

Degree: Master of Science

We present an investigation of the reaction dynamics of Cl radicals with butane in crossed beams, were studied at two collision energies: ~ 6.5 and 9 kcal/mol. Product were ionized using a 157 nm probe laser, and detection was through a dc slice detection setup. The translational energy distribution integrated over all scattering angles; look similar for both collision energies. The angular distribution shows that at high collision energy the there is a sharp increase in the forward scattering. At low collision energy there is more backscattering. The results show that the different scattering angles give different translational energy distribution. The forward scattered peaks at approximately 85% of the collision energy, with a similar distribution for both collision energies. The sideways-scattered product shows the broader distribution that extends into higher energy. The back-scattered product showed the broadest distribution and a higher fraction of total energy showing up in translational energy.

AUTOBIOGRAPHICAL STATEMENT

I was born in Baalbek, Lebanon on July 19th, 1978. My family and I lived there until 1988 when we immigrated to Canada. After I turned fourteen, we returned to my birth country's next door neighbor, Syria where I graduated from high school. College took me from The Middle East to The Midwest, Lincoln Nebraska to be exact. Right after college, I got my first career related job in Pittsburgh, PA for Pittsburgh Plated Glass. In 2007 I got married to an amazing girl from back home with whom a year later my gorgeous daughter was born. I hope to move back to the Middle East after graduation to work on developing renewable energy projects.